



Enhanced supercapacitor performance through synergistic electrode design: Reduced graphene oxide-polythiophene (rGO-PTs) nanocomposite

Anita K. Tawade^a, Shivaji N. Tayade^b, Deepak P. Dubal^c, Sawanta S. Mali^d, Chang Kook Hong^d, Kiran Kumar K. Sharma^{a,*}

^a School of Nanoscience and Biotechnology, Shivaji University, Kolhapur 416004, MS, India

^b Department of Chemistry, Shivaji University, Kolhapur 416004, MS, India

^c School of Chemical Engineering, The University of Adelaide, Adelaide, South Australia 5005, Australia

^d Department of Advanced Chemical Engineering, Chonnam National University, Gwangju, 61186 South Korea



ARTICLE INFO

Keywords:

Conducting polymer
Supercapacitor
Graphene oxide functionalization
Swollen Liquid Crystalline Lamellar Mesophase
Galvanostatic- Charge discharge

ABSTRACT

In this investigation, we introduce an innovative method for the fabrication of a 2D/2D nanocomposite, involving the in-situ functionalization of graphene oxide (GO) with thiophene monomer. This approach employs a modified surfactant-based bi-solvent swollen liquid crystalline lamellar mesophase (SLCLM) nanoreactor system, utilizing dimethyl sulfoxide and water as primary solvents. The nanocomposite is formed via simultaneous reactions at both the edge and basal plane of GO with thiophene monomers, resulting in polymerization and reduction to generate graphene oxide-polythiophene (rGO-PTs) nanocomposite.

We assess the pseudocapacitive properties of rGO-PTs in a 2 M HCl electrolyte. The cyclic voltammetry (CV) investigations reveal distinctive redox curves, indicative of the materials capacitive behaviour. In the galvanostatic charge-discharge (GCD) study, the rGO-PTs exhibits a discharge duration of 169.50 s within a potential window of -0.2 to 1 V at a current density of 7.5 A/g. This performance corresponds to a significantly higher specific capacitance of 1412 F/g, sustained over 10000 cycles as asymmetric capacitor. Notably, the rGO-PTs nanocomposite retains 106 % of its initial capacitance even after a number cycles, tested at a scan rate of 50 mV/s. The exceptional durability and electrochemical performance of the rGO-PTs nanocomposite position it as a promising alternative to conventional materials such as metals, metal oxides, pure carbonaceous substances, and polymers. The simplicity of the synthesis process, coupled with the nanocomposites outstanding electrochemical characteristics, underscores rGO-PTs potential for advancing in the field of energy storage and supercapacitor technology.

1. Introduction

In recent years, critical challenges have emerged in the energy sector i.e. conventional and non-conventional energy resources are insufficient to meet escalating global energy demands. This ongoing crisis is further intensified by the environmental impact caused due to natural fuel and coal consumption, which produces greenhouse gases. In response, the quest for efficient, high-power energy sources has intensified, with a noticeable surge in research interest in the field of electrochemical supercapacitors. These devices are known for their long life cycles, rapid charge storage, and high power density, thus, is increasingly viewed as a vital addition to the existing fuel cells, conventional batteries, and conventional capacitors [1].

Electrochemical supercapacitors are broadly classified into two types: electrical double-layer capacitors (EDLCs), which utilize carbon material for charge storage, and pseudocapacitors, which are characteristics of metal oxides and conducting polymers, facilitating fast and reversible redox reactions [2]. To optimize power and energy density, researchers have focused on composite supercapacitor electrodes, blending carbon-based materials with metal oxides, or conducting polymers. Despite their higher energy densities, pseudocapacitive devices face challenges in longevity and power density, primarily due to phase changes and faradaic reactions [3]. Addressing these limitations, recent studies have focused on conducting polymer composites, such as PANI/inorganic nanocomposites, graphite/PPy composites, and PANI/activated carbon [4]. Among the conducting polymers, polythiophene

* Corresponding author.

E-mail address: kks.snst@unishivaji.ac.in (K. Kumar K. Sharma).

(PTs) stands out owing to high electrical conductivity, significant characteristics of a pseudocapacitance, high energy density, affordability, and eco-friendly [5].

Carbon-based materials are predominantly used in supercapacitor (SC) as electrodes due to their relatively low cost, excellent electrical conductivity, and high surface area, making them well-suited for rapid energy storage and release. Graphene, characterized by the long aromatic conjugated backbone composed of sp^2 -hybridized carbon atoms in a single layer, exhibits outstanding optical, mechanical properties and versatility [6]. However, applications in aqueous medium are limited due to the inherent hydrophobic nature, because of the absence of oxygen functional groups in graphene. The superior electrochemical performance as micro-supercapacitors of 3D-printed graphene-based aerogel architecture assembly has been attributed to the efficient ion transport facilitated by the interconnected networks within the structure [7]. Further, a graphene (Gr)-bridged based heterostructure device of the type semiconductor/Gr-bridge/n-type molybdenum disulfide has been developed as a channel material for field-effect transistors (FET), which opens the potential of designing high-end application devices in the field of ambipolar semiconductors [8]. In a recent study, graphene oxide has been used as interlayers to augment the flexibility of MXene multifunctional films including electrochemical supercapacitance [9].

Graphene oxide (GO), a crucial derivative of graphene, is distinguished by its layered structure, with oxygen-containing functional groups present on its basal planes and edges. This induces a hydrophilic character to GO, in contrast to the hydrophobic nature of graphene [10]. Thus, the dispersion of GO in water is much easier than that of graphene leading to the synthesis of GO composites with metal oxides and conducting polymers.

Subsequent research focused on the fabrication of RGO/polyaniline (PANI)/urchin-like mesoporous TiO_2 sphere composites, revealing higher capacitance of 464 F/g at a current density of 0.62 A/g [11]. The synthesis of sodium phytate-doped 3D PANI nanofibers attached to carbon paper substrates, displayed excellent specific capacitance of 1106.9 ± 1.5 F/g and 779 ± 2.6 F/g at current densities of 0.5 and 10 A/g, respectively. The symmetric supercapacitor assembly demonstrated significant improvement in both energy density and power density, yielding 95 Wh/kg at 846 W/kg [12]. In addition, as synthesized reduced graphene oxide-polyaniline-bio waste derived activated carbon [PANI@OS – rGO (1:1)] hybrid electrode exhibited electrochemical capacity of 582.6 F/g at a current density of 0.1 A/g and an energy density of 26.82 Wh/kg, indicating promising potential for effective energy storage. [13]. The specific capacitance (C_{sp}) of reduced graphene oxide/poly(pyrrol-co-thiophene) (RGO/COP) was determined to be 467 F/g from CV measurements and 417 F/g from GCD experiments at a current density of 0.81 A/g. The energy density was determined to be 86.4 Wh/kg, coupled with a power density of 630 W/kg. Notably, the hybrid composite shows favourable cyclic stability, retaining 65 % of its capacitance after undergoing 1000 cycles at a scan rate of 100 mV/s [14]. In a one-pot synthesis, Wang et. al. synthesized a metal oxide-reduced graphene oxide-conducting polymer (SnO_2 /RGO PEDOT) based composite having a specific capacitance of 184 F/g at 1 mV/s, displaying promising results during cycling tests with a remarkable 114 % enhancement in capacitance retention after 5000 cycles at a charge-discharge current density of 10 A/g [15]. A ternary poly (3,4-ethylenedioxythiophene)-poly-(styrenesulfonate) (PEDOT:PSS)-wrapped tin oxide/reduced graphene oxide (SnO_2 /RGO/PEDOT: PSS) known as SGP nanocomposite electrode, operating within a wide voltage window of -0.6 V to $+0.6$ V, exhibited a maximum specific capacitance of 285.0 F/g at a scan rate of 1 mV/s. This superior performance suggests a potential application in future energy storage devices with high operating voltage. The SGP-based supercapacitor demonstrated significantly higher energy density of 17.7 Wh/kg and a power density of 1220 W/kg [16].

In this study, we investigate, for the first time, the application of a 2D/2D nanocomposite comprising graphene oxide (GO) and

polythiophene (PTs) fabricated in a surfactant based swollen liquid crystalline lamellar mesophase (SLCLM). This approach tries and addresses certain gap in the current understanding in the designing and synthesis of GO based nanocomposites, where the available literatures predominantly assigns to the physical interactions between the reactants/nanomaterials and GO functional groups [17]. Our strategy aims to overcome the inherent structural challenges associated with GO by preserving the two-dimensional morphology and the orientation of the functional groups in the basal and edge planes during the synthesis process. Maintaining these conditions is pivotal for achieving uniform chemical modifications across the GO structure. The innovative use of the SLCLM method enables the retention of the 2D morphology and orientation functional groups of the GO, facilitating simultaneous nucleophilic reactions, essential for the chemical transformations to occur. Consequently, the synthesized rGO-PTs nanocomposite demonstrates enhanced specific capacitance and energy density in comparison to pure GO and exhibits higher specific capacitance and power density relative to polythiophene in hydrochloric acid electrolyte. The electrochemical performance of this material is comprehensively evaluated using electrochemical techniques like cyclic voltammetry (CV), galvanostatic charge–discharge (GCD), and electrochemical impedance spectroscopy (EIS). The findings of this study indicates rGO-PTs nanocomposite is an emerging and a promising candidate for supercapacitor applications, exhibiting a remarkable specific capacitance of 1412 F/g after 10000 cycles.

2. Experimental

2.1. Materials

Thiophene (C_4H_4S , $\geq 99\%$), Cyclohexane (99.5 %), 1-pentanol ($\geq 99\%$) and Iron (III) chloride (98 %), were purchased from Sigma Aldrich. Potassium permanganate ($KMnO_4$, 99.5 %) Cetylpyridinium chloride ($CpCl$, SRL, 98 %) were purchased from SRL. Iso-propyl alcohol (99 %) is purchased from Molychem. Graphite flakes (150 μm , $\geq 99.99\%$), Phosphoric acid (Extra pure H_3PO_4 , 88 %,) were purchased from SDFCL. Dimethyl sulphoxide (DMSO, 99 %), Potassium persulphate ($K_2S_2O_8$, 99 %), Sulphuric acid (H_2SO_4 , 90 %), Hydrogen peroxide (H_2O_2 , 30 %), Hydrochloric acid (Analytical Grade, 98 %,), Diethyl Ether (99 %) were purchased from Thomas Baker. Ethanol (Absolute, $\geq 99\%$) is purchased from Changshu Hongsheng Fine Chemicals Co. Ltd.

All solutions was prepared using double distilled water from a Borosil all Quartz Double Distillation Unit.

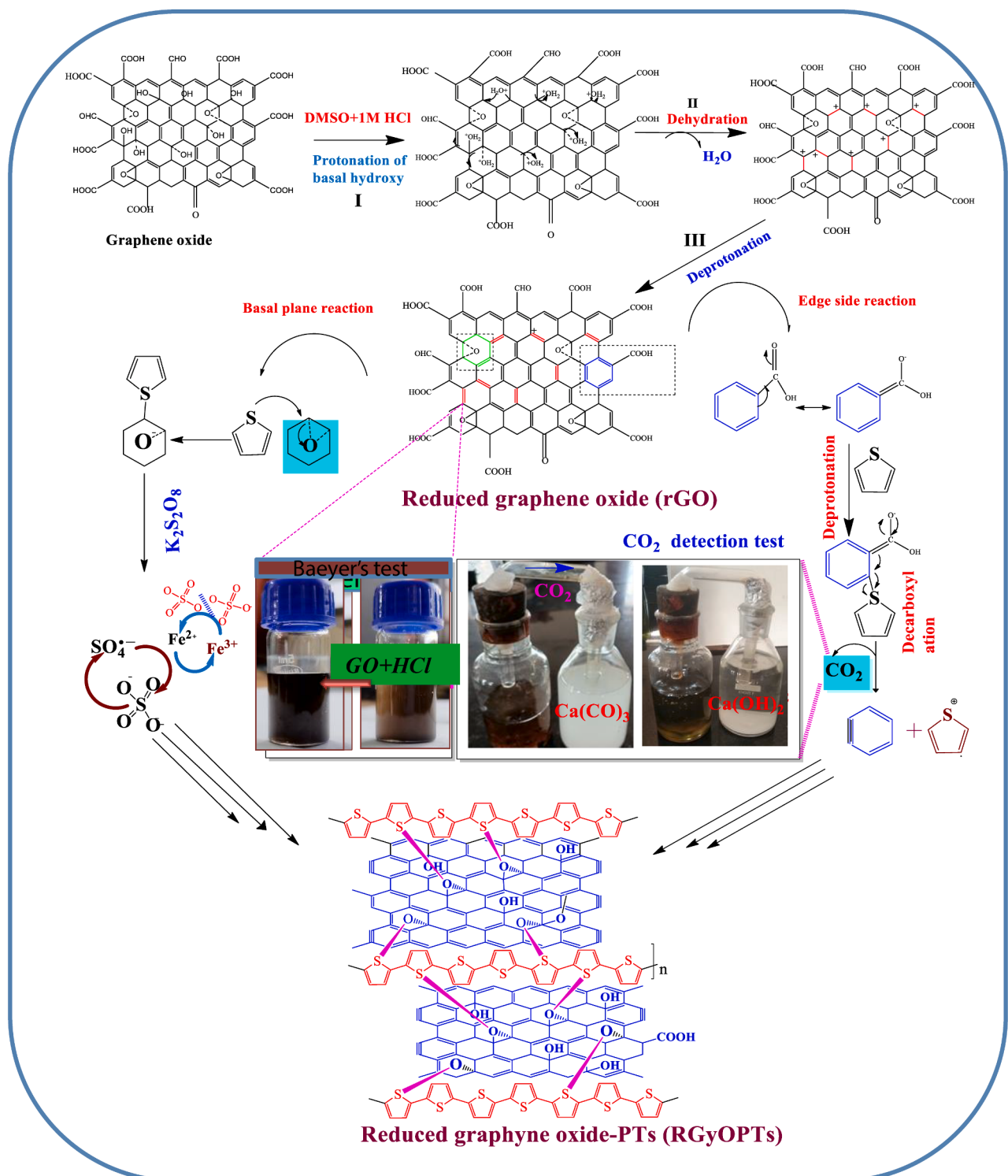
2.2. Synthesis of rGO-PTs nanocomposite in swollen liquid crystalline lamellar mesophase (SLCLM)

Graphene oxide (GO) was prepared using an improved version of the Hummers' method, known for its efficacy in chemical exfoliation [18]. For the synthesis of reduced graphene oxide-polythiophene (rGO-PTs) nanocomposite, a surfactant based swollen liquid crystalline (SLC) mesophase template was employed. The initial step involves creating a mesophase by dissolving 1.47 M cetylpyridinium chloride ($CpCl$) in 2 ml of 1 M HCl solution prepared using double distilled water (ddw) and addition of 3 ml of cyclohexane and vigorous vortexed, resulting in a viscous and turbid micellar mixture. 1-pentanol (400 μl) was added as a co-surfactant to the micellar mixture until a clear hexagonal mesophase visible with naked eye was formed. Subsequently, 0.22 mg/ μl of the synthesized GO, dispersed in dimethyl sulfoxide (DMSO) was added to the hexagonal mesophase and vigorously vortexed. This was followed by the addition of 9.05 M of thiophene monomer and 0.44 M of potassium persulfate as oxidising initiator, to the above mixture. The reaction mixture was further subjected to constant vortex for 15 min., leading to the formation of a white, unstable emulsion. Further addition of 200 μl of 1-pentanol transformed this emulsion into a transparent and stable lamellar mesophase, identified by naked eye. The final step involved

addition of 1.97 M ferric chloride (FeCl_3) as catalyst into the lamellar mesophase. This addition caused a rapid colour change of the lamellar mesophase from yellow to dark brown, indicating the progression of the reaction. The lamellar mesophase was then left in the dark for 24 h and allowed to polymerize. The product was isolated by destabilizing the lamellar mesophase using isopropyl alcohol (IPA) followed by centrifugation at 8000 rpm for 10 min. The isolated product was further washed successively using IPA and dddw to remove any unreacted monomers and CpCl at large. The extracted product was finally dried in

a hot air oven at 60 °C for 24 h, yielding the desired rGO-PTs nanocomposite.

The formation of rGO-PTs nanocomposites involves a complex mechanism, which is elucidated in **Scheme 1**. This mechanism initiates with the protonation of hydroxyl groups on the basal plane of graphene oxide (GO) in dimethyl sulfoxide (DMSO), leading to the generation of an alkyloxonium ion (as shown in Step I) [19] which further undergoes a spontaneous dehydration reaction, coupled with a deprotonation process, increasing the sp^2 carbon content, thereby enhancing the



Scheme 1. Proposed mechanism of basal dehydro-deprotonation of GO with possible formation of reduced graphyne oxide (RGyOPTs) nanocomposite.

conjugation within the GO structure (Steps II and III) and transformation to reduced graphene oxide (rGO). These reactions occurs predominantly at the basal (epoxy, $-OH$) and edge ($-C = O$, $-CHO$, and $-COOH$) functional groups of the GO.

The generation of the product, rGO-PTs involve in-situ polymerization process within the swollen liquid crystalline lamellar mesophase (SLCLM), where thiophene acts as a nucleophile. This facilitates simultaneous nucleophilic substitution and elimination reactions with the GO's basal and edge functional groups. The increase in conjugation due to new $-C = C-$ bond formation in GO is evident from the Baeyer's test, where 1 % $KMnO_4$ was added dropwise to a GO dispersed in HCl mimicking the condition in SLCLM and observed the disappearance of pink colour indicating the presence of unsaturated groups in GO + HCl solution (upper left-side image in Scheme 1). Thus, the in-situ formation of reduced graphene oxide (rGO) in the SLCLM reaction condition is explained which is also complemented by the XRD diffraction pattern and Raman spectrum analysis (Fig. 1).

The in-situ generated rGO further undergoes reactions, including the possible epoxide ring opening and polymerization of thiophene monomers. The reaction between thiophene monomers and epoxide functional groups on the basal plane of the GO is proposed for the formation of covalent $-S-O-$ bonds between rGO and thiophene (Basal plane reaction, Scheme 1). Concurrently, another simultaneous reaction on the functional groups involves dehydrogenation followed by decarboxylation reaction (Edge side reaction, Scheme 1) is proposed for the possible formation of acetylenic ($-C \equiv C-$) bonds. This results in new acetylenic edges and sp^2 carbons, characteristic of graphyne structures [20,21]. CO_2 evolution during synthesis in SLCLM is confirmed by a lime water test which turns clear $Ca(OH)_2$ solution to with precipitation of

$CaCO_3$ as shown in the right-side image of Scheme 1.

The in-situ synthesis also involves Fe^{3+} catalysed generation of sulphate radical anion oxidant in the SLCLM system as shown in the bottom left panel of the Scheme 1. Thiophene polymerization within the lamellar mesophase occurs when the persulphate ion ($S_2O_8^{2-}$) substitutes chlorine in $CpCl$. The persulphate anion is then oxidized by Fe^{3+} ion to produce sulphate radical anion ($SO_4^{2\bullet-}$). This leads to the formation of a thiophene cation radical and a sulphate cation radical, which initiates polymerization of thiophene monomers producing polythiophene (PTs) in the SLCLM. The reaction of the sulphate cation radical with Fe^{2+} (from the initial conversion of $S_2O_8^{2-}$ to $SO_4^{2\bullet-}$) regenerates Fe^{3+} and sulphate anion, thereby recycling the initiator for ongoing polymerization.

2.3. Characterization

The crystallographic structures of the synthesized nanomaterials were determined using an X-ray diffractometer (Rigaku D/max 2550 Pe) equipped with $Cu K\alpha$ monochromatic radiation (wavelength: 1.54 Å) operating at 40 kV and 300 mA over a 20 range of 5 to 80°. Fourier-transform infrared (FT-IR) spectra of the synthesized nanomaterial were recorded using a Bruker FT-IR-6600 spectrometer, spanning a spectral range of 400–4000 cm⁻¹. The morphology, including the size and shape of the nanomaterials, was analyzed with a high-resolution transmission electron microscopy (HR-TEM), JEOL JEM F-200 microscope, which features a Schottky field emission gun and offers a point-to-point resolution of approximately 2 Å. X-ray photoelectron spectroscopy (XPS) measurements were conducted on a Thermo Scientific K alpha + spectrometer, employing micro-focused, monochromatic Al $K\alpha$

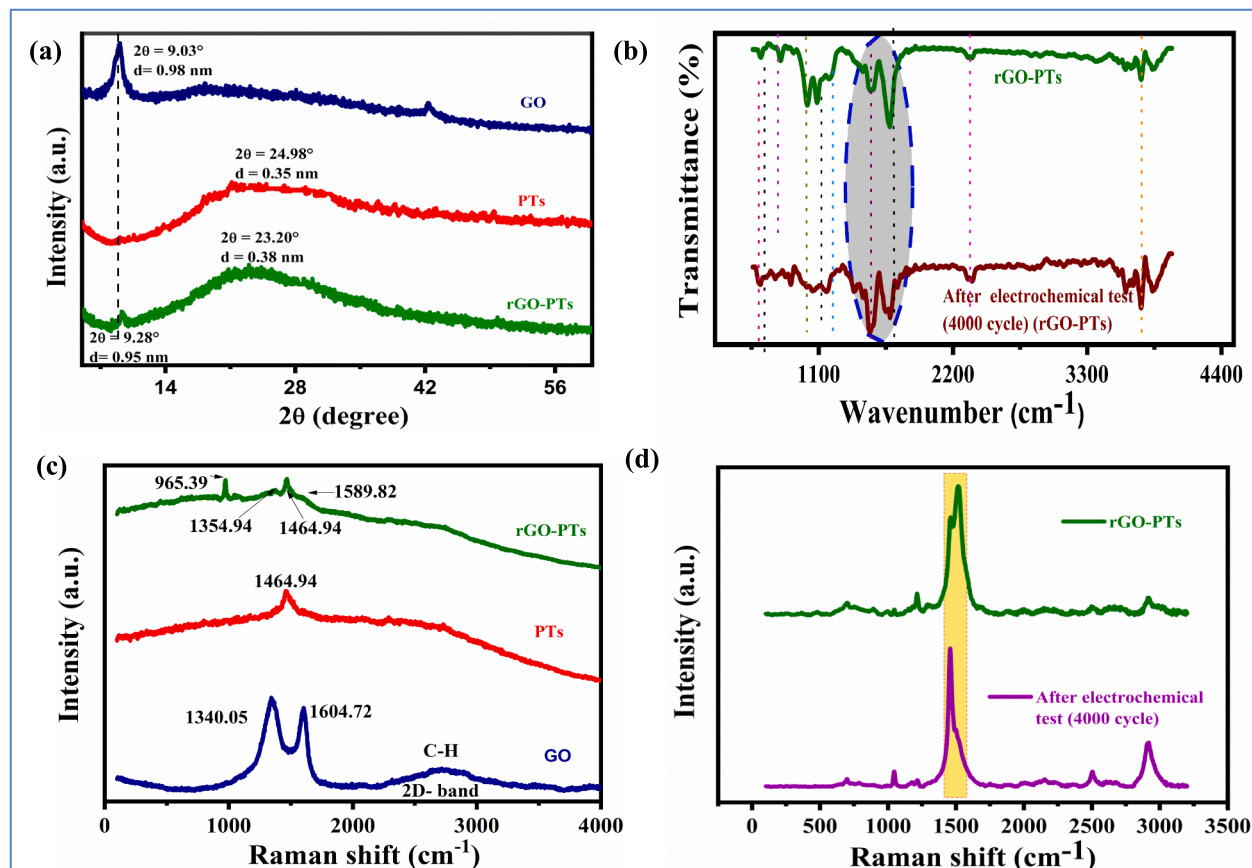


Fig. 1. (a) XRD pattern of synthesized GO, PTs and rGO-PTs. (b) FT-IR spectra of as prepared rGO-PTs and rGO-PTs after electrochemical test (4000 cycles). (c) Raman spectra of GO, PTs, rGO-PTs. (d) Raman spectra of as prepared rGO-PTs nanocomposite modified electrode and the same electrode after the electrochemical tests.

radiation (energy: 1486.6 eV) with a spectral acquisition pass energy set to 50 eV for individual core-level analyses. The Raman spectra were obtained using a HORIBA Raman spectrometer, utilizing a 632 nm laser as the excitation source. Solid-state ^{13}C CP-MAS NMR analysis were performed using a JEOL 400 spectrometer (operating frequency: 400 MHz) with a probe (H164388_0001 PH MAS DVT 500 W2 BL4 N-P/F/H) and employing a cross-polarization (cp) pulse sequence. The specific surface area and pore size distribution of the nanomaterial were measured using nitrogen adsorption-desorption isotherms, with Brunauer–Emmett–Teller (BET) and Barrett–Joyner–Halenda (BJH) methods, on a Quantachrome Autosorb 1-MP analyzer.

The electrochemical properties of the synthesized nanomaterial were evaluated using cyclic voltammetry (CV), potentiostatic electrochemical impedance spectroscopy (EIS), and galvanostatic charge–discharge (GCD) techniques. These techniques were performed using a three-electrode cell configuration, containing 2 M HCl as electrolyte, on a Metrohm Autolab PGSTAT 302 N potentiostat/galvanostat. The cell comprises a modified glassy carbon electrode (GCE, diameter 3 mm) coated with the as synthesized nanomaterial as the working electrode, a platinum wire as the counter electrode, and a saturated KCl Ag/AgCl electrode as the reference.

3. Results

Crystalline nature of GO, PTs and rGO-PTs was analyzed by using X-ray diffraction patterns. Fig. 1a shows a characteristic sharp peak centered at 2θ value of 9.03° of the as synthesized pristine GO corresponding to a (001) reflection plane. The interlayer spacing of GO was calculated at 0.98 nm. For the as synthesized pristine PTs, the XRD pattern showed broad, amorphous diffraction peak at 2θ = 24.98° having d spacing of 0.35 nm as depicted in Fig. 1a. This diffraction pattern characterizes strong association with the π–π stacking structure in polythiophene chains. A broad band is observed at 23.20° corresponding to a d spacing of 0.38 nm in the as synthesized rGO-PTs nanocomposite which is lower than that observed for pristine PTs. Similarly, the GO peak is shifted towards higher 2θ (9.28) with d spacing of 0.95 nm as compared to the pristine GO. Thus, XRD analysis confirms the retention of amorphous structure PTs after the modification on the surface of the rGO [22], which co-relates interlayer spacing to the degree of oxidation. The XRD pattern of the rGO-PTs nanocomposite further proves the complete oxidation of graphite intercalated compound (GIC) samples [23]. Additionally, the polar functional groups of GO promotes direct intercalation of hydrophilic molecules, with the interlayer spacing increasing the uptake of monomer or polymer [24].

FTIR spectra of GO and PTs are explained in detail in Supporting information with Figure S1. Fig. 2b shows the FTIR spectra of as prepared rGO-PTs and after GCD test (4000 cycles). FTIR spectra of rGO-PTs shows characteristic peaks of PTs can be observed at 1084 cm⁻¹ and 1196 cm⁻¹. These peaks represent stretching vibrations of the thiophene ring [25]. The peak at 1093 cm⁻¹ and 1196 cm⁻¹, 1523 cm⁻¹, represent sulphur-oxygen, –C-S-C- and carbon–oxygen bonds of polythiophene. In case of rGO-PTs nanocomposite after GCD test, a small shift is observed in two major peaks corresponding to 1037 cm⁻¹, 1153 cm⁻¹. In generally, a lower shift in the wavenumber indicates the increasing bond length and vice versa. These peaks are identified as –C=C– bonding at 785 cm⁻¹ and 899 cm⁻¹ [26]. A broad peak at 3635 cm⁻¹, 3744 cm⁻¹ and 3865 cm⁻¹ corresponds to –OH stretching vibrations of the –C-OH group and water content in the material. A strong peak appears at 1670 cm⁻¹ before electrochemical test these bond appears very sharp and strong as compared to after rGO-PTs after GCD electrochemical test, which can be assumed to be the result of reduction in the oxygen containing functional groups, which is complemented by XPS analysis where oxygen content after GCD cycles is found to be reduced. High electronegativity of the rGO molecules could be responsible for this increased in bond length in the thiophene ring of rGO-PTs nanocomposite after electrochemical performance.

It is well known that the D band, which is prominent, is due to disordered structural defects and the G band ascribed to the first-order scattering of the E_{2g} mode observed for sp² carbon domains (e.g. amorphous carbon or edges that can break the symmetry and selection rule). The Raman spectra indicates decrease in the I(D)/I(G) ratio of pristine GO upon the introduction of PTs as well as a red shift of the peak positions is observed. From Fig. 1c, the Raman spectra of GO shows ID/IG 1.12, sharp G band at 1602 cm⁻¹ with higher intensity than the D band at 1344 cm⁻¹ which are in agreement with highest % of sp² carbon atoms and 2D band at 2737 cm⁻¹ [27]. The 2D band appears in GO as a doublet (Fig. 1a) due to the splitting of the π and π* electronic states, owing to the interactions between the successive GO layer planes. The Raman spectrum is quasi indistinguishable from that of graphite, i.e., the 2D band splitting merge into a double [28]. The most intense band, at around 1467 cm⁻¹, can be attributed to symmetric in-phase vibration of thiophene rings dispersed across the entire polymer chain [29]. The Raman band around 1467 cm⁻¹ is assigned to conjugated polythiophene segments (C_α = C_β) ring stretching in the neutral state. Raman spectrum of rGO-PTs nanocomposite shows blue shift in D band and red shift in G band as compared to pristine GO (ID/IG = 1.07). The comparison of ID/IG ratio between nanocomposite and GO shows strong enhancement of sp² carbon characteristics which is attributed to the decrease in oxygen density confirm from XPS spectral binding energy data for C 1 s, O 1 s and S 2p. The peak at 1357 cm⁻¹ is assigned to the bipolaron absorption; the band of Cβ-H bending appears at 966 cm⁻¹. The peak at about 1360 cm⁻¹ assigned to be Cβ' – Cβ' ring stretching belongs to the same species of PTs band at 1468 cm⁻¹ is attributed to the another species of PTs [30]. The blue shift can be attributed to the bonding between thiophene rings and six-member rings of rGO as well as intercalation of thiophene sheet between successive sheets of rGO.

The Raman spectra of the rGO-PTs nanocomposite, as depicted in Fig. 1d, were analyzed after 4000 charge–discharge cycles ranging from –0.2 to 1 V. A notable enhancement in the D band, observed at 1457 cm⁻¹ and is proposed to the formation of smaller graphene sheets [31]. Specifically, it suggests the development of graphene-like sp² domains that are smaller in size compared to those in the electrochemically pre-treated sample [32]. This observation supports the hypothesis that the rGO is primarily amorphous state, with a graphite-like state being recovered only upon reduction. Following the reduction of GO, there is a shift in the D and G bands to 1351 cm⁻¹ and 1599 cm⁻¹, respectively. These shifts are indicative of structural changes in the material, aligning with the formation and transformation of graphene-related structures within the nanocomposite [33].

Comprehensive X-ray photoelectron spectroscopy (XPS) analysis of pristine graphene oxide (GO), pristine polythiophene (PTs), and the rGO-PTs nanocomposite are depicted in the Supporting information Figure S2. The comparative XPS spectra of the as-prepared rGO-PTs nanocomposite and after 4000 cycles of galvanostatic charge–discharge (GCD) are depicted in Fig. 2. The C 1s region in both the samples is obtained by deconvolution of the spectrum into five distinct peaks, each representing different carbon-associated functional groups: carbon in sp² hybridization (–C = C-, at 284.25 eV), sp³ hybridization (–C-C-, at 284.92 eV), epoxy/hydroxyl groups (–C-S-, at 286.02 eV), ether groups (–C-O-C-, at 287.70 eV), and carbonyl groups (–C = O-, at 288.50 eV).

Notable transformations are evident in the C 1s spectra of the pristine GO following the incorporation of PTs, as detailed in the Supporting information (Figure S2b). In Fig. 2 (a, b), the reduction of oxygen functionalities within the core C 1s spectra is apparent. There is a marked increase in the ratio of carbon–carbon bonds relative to epoxy/hydroxyl/-C-S- and carboxylate groups, indicating successful integration of carbon groups during the synthesis as tabulated in Table 1. This trend also suggests an increase in sp² hybridized –C = C- bonds, indicative of the formation of graphitic carbon structures [30].

Additionally, the emergence of a distinct peak attributed to sulphur (S 2p) after the 4000 cycles of GCD, potentially in the form of SO₃²⁻, corresponds to a sulphur presence of 5.75 % on the samples surface. This

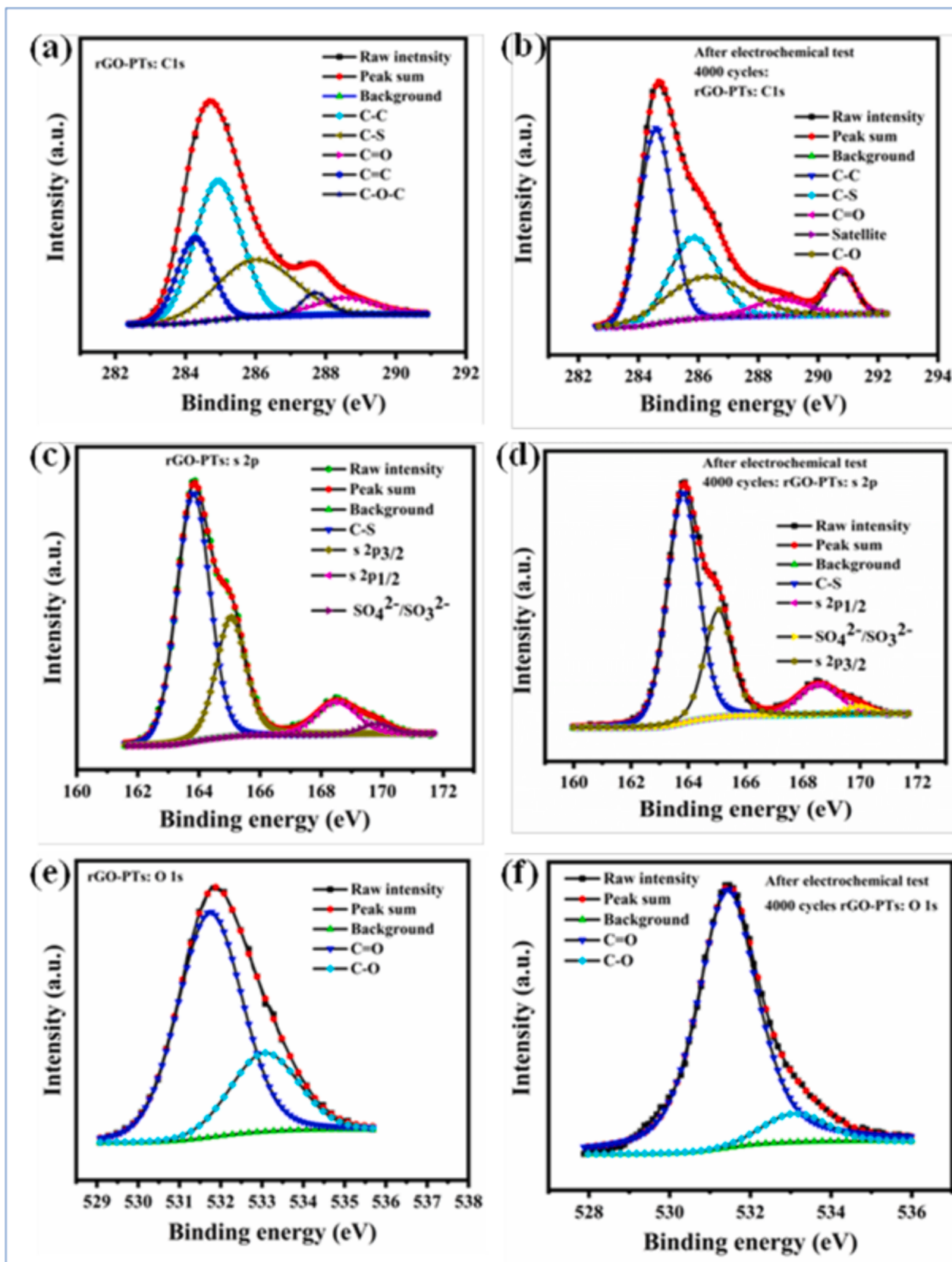


Fig. 2. (a) XPS spectra rGO-PTs: C 1s (b) rGO-PTs: S 2p. (c) rGO-PTs: O 1s. (d) rGO-PTs after electrochemical test (4000 cycles) rGO-PTs: C 1s. (e) after 4000 cycles rGO-PTs: S 2p and (f) rGO-PTs: O 1s after electrochemical test.

Table 1

The atomic percentage of characteristic peaks of XPS spectra of GO, PTs, rGO-PTs and after electrochemical test (4000 cycles).

Materials	O 1 s	C 1 s	S 2p
GO	35.97	61.83	1.66
PTs	22.39	64.73	12.25
rGO-PTs	21.89	66.06	11.31
After 4000 cycles	18.18	74.86	5.75

observation suggests sulphur accumulation during the electrochemical reduction process of the prepared electrode, underscoring the effective incorporation of sulphur from PTs into the rGO-PTs structure.

The core-level X-ray photoelectron spectroscopy (XPS) spectra for carbon (C 1 s), oxygen (O 1 s), and sulphur (S 2p) levels of the sample were sequentially recorded over a sputtering duration ranging from 0 to 840 s, employing argon ion bombardment for the depth profiling. The sputtering rate was 0.015 nm/s (15 pm/s), with each etching interval set at 15 s. The primary goal of this approach was to establish a correlation between the quantification values and the etching duration. The sample under investigation comprised of a multilayer structure, alternating between rGO and polythiophene layers, deposited atop a silicon wafer substrate. It was noted that the etching rates might differ between layers, particularly between those rich in carbon and sulphur, with potential variations upon reaching the silicon substrate.

The XPS spectra, specifically the C 1 s, S 2p, and O 1 s regions, are illustrated in Fig. 3 (a, b, c). In these spectra, the C 1 s peaks exhibited greater intensity in the carbon-rich layers as compared to the sulphur

layers, as indicated in Fig. 3d. The O1s spectra in Fig. 3c revealed minimal surface oxidation of rGO-PTs, with a noticeable shift in oxygen binding energy towards lower values, suggesting electron transfer from polythiophene to reduced graphene oxide. The analysis of the S 2p spectra revealed a gradual decrease in the intensity of peaks corresponding to $\text{Sp}_{3/2}$ and $\text{Sp}_{1/2}$ with increased sputtering time. Similarly, the intensity of the SO_3^{2-} peaks diminished over the course of sputtering, remaining constant for the initial 440 s but then decreasing sharply with extended etching up to 840 s. This trend indicated that sulphur atoms, being less volatile and heavier than carbon atoms, experienced a relatively higher etching rate. Notably, the sputter etching led to a significant change in the line shape of the S 2p peak, merging the $2\text{p}_{1/2}$ and $2\text{p}_{3/2}$ levels into a single broadened peak after 15 s of etching, highlighting the substantial impact of Ar-ion etching on sulphur levels.

The observed fluctuations in peak intensity relative to the sputtering time suggested the presence of alternating 2D/2D sheets of sulphur and carbon within the rGO and polythiophene layers. This structural composition was further complemented by field emission scanning electron microscopy (FE-SEM) and high-resolution transmission electron microscopy (HR-TEM) images.

Fig. 4 depicts the high-resolution transmission electron microscopy (HR-TEM) images of graphene oxide (GO) (a-b), polythiophene (PTs) (c-d), and the rGO-PTs nanocomposite (e-f). Detailed HR-TEM analysis, as depicted in Fig. 4 (a-f), substantiates the successful fabrication of the rGO-PTs nanocomposite. The HR-TEM images of GO, shown in Fig. 4 (a-b), reveal dark regions representing the densely stacked nanostructures of multiple graphene oxide layers, interposed with oxygen functional groups. Fig. 4b highlights higher transparency fringes, indicative of

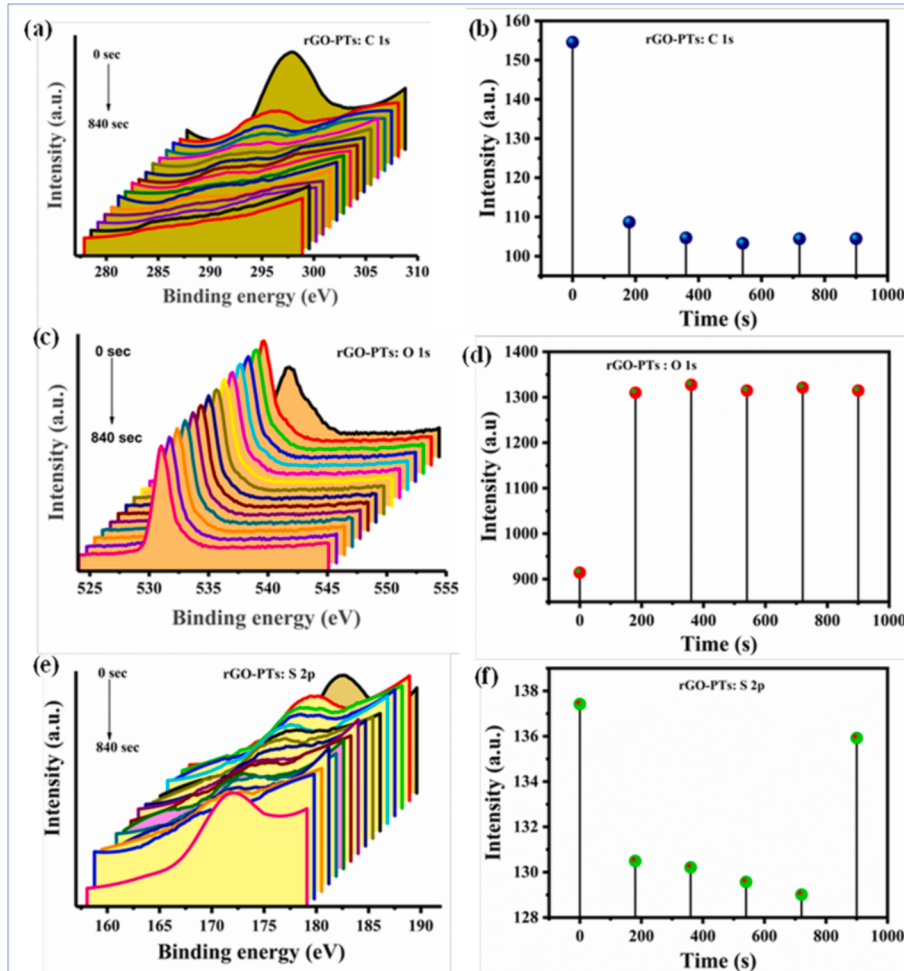


Fig. 3. 3D XPS depth profiles of rGO-PTs nanocomposite (a) C 1 s. (b) S 2p. (c) O 1 s and (d, e, f) graph of different sputter etched time (s) Vs. intensity.

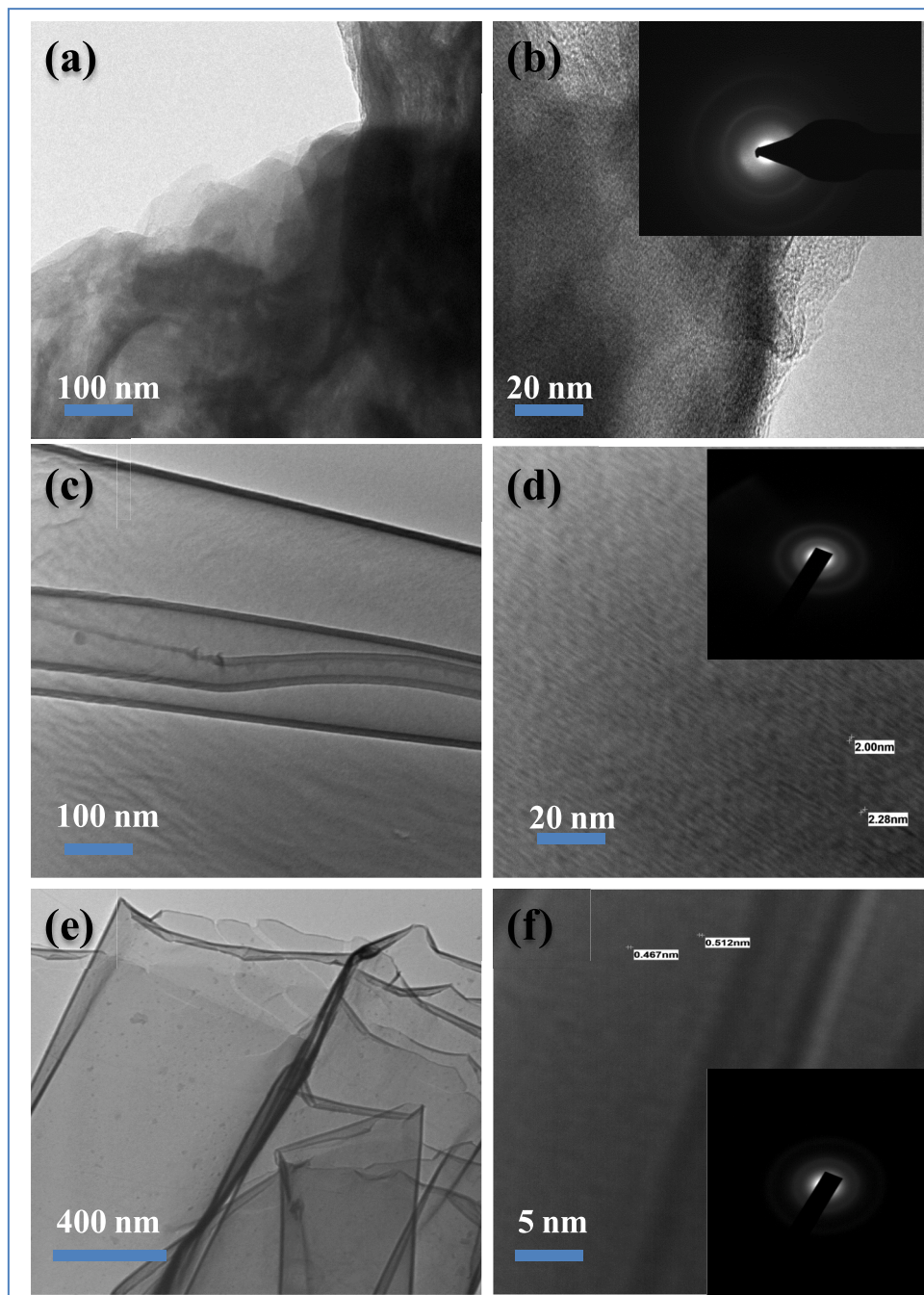


Fig. 4. HR-TEM images of GO (a-b), PTs (c-d) and rGO-PTs (e-f) nanocomposite.

much thinner films comprising a few layers of graphene oxide, a result of the exfoliation of the stacking nanostructure. The accompanying selected area electron diffraction (SAED) inset in Fig. 4b demonstrates pristine GO possesses a less amorphous structure compared to pristine PTs and the nanocomposite.

The morphology of PTs, as observed in the HR-TEM images, features randomly sized bare nanosheets. A high-resolution image of these large nanosheets, around 20 nm in width (Fig. 4c), exhibits a highly amorphous lattice fringe with spacing ranging from 2 to 2.30 nm. The SAED analysis in Fig. 4d confirms the amorphous nature of the PTs nanosheets. Fig. 4 (e-f) show case the 2D/2D morphology of the rGO-PTs nanocomposite, illustrating that the PTs film consists of well-aligned, stacked sheets of rGO and PTs, arranged layer by layer. The PTs sheets are uniformly intercalated between successive layers of GO. A notable

observation in the rGO-PTs nanocomposite is the reduction in fringe size compared to pristine PTs, with spacing of approximately 0.51 and 0.40 nm, respectively. The SAED pattern of the nanocomposite further indicates its amorphous character.

Fig. 5 illustrates the N_2 adsorption-desorption isotherms and the corresponding pore size distribution curves of pristine GO, PTs and rGO-PTs nanocomposites. Following the IUPAC classification, all the adsorption-desorption isotherms exhibited type IV curves with a clear H1 hysteresis loop, which reflects the mesoporous structures existing in the synthesized rGO-PTs nanocomposites as well as facile connectivity between the pores. The specific surface area, pore volume, and pore size of different samples were calculated, and the data are summarized in Table S1. For pristine GO, PTs and rGO-PTs nanocomposites the specific surface area are determined with values corresponding to 78.54, 64.81,

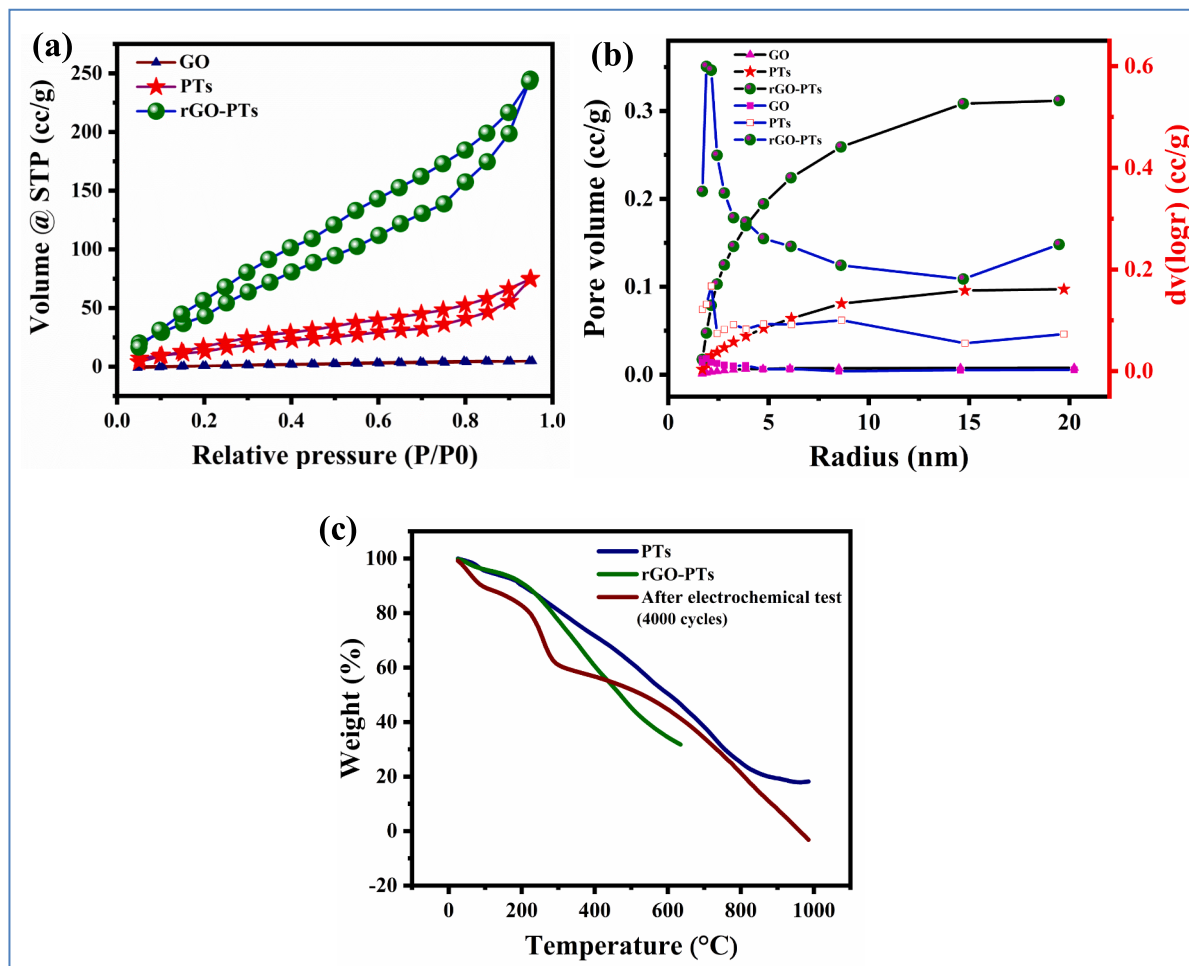


Fig. 5. (a) Nitrogen adsorption–desorption isotherms of GO, PTs and rGO-PTs. (b) Pore size distribution of pristine GO, PTs and rGO-PTs. (c) Thermogravimetric analysis curves of GO, PTs and rGO-PTs. nanocomposites.

236.71 m²/g respectively. As can be seen, the rGO-PTs nanocomposite has 3–4 folds increased in specific surface area. Similarly, the total pore volumes are 0.007, 0.116, 0.378 cc/g and the average pore sizes are 3.19, 3.58, 3.20 nm, respectively.

It is interesting to observe that when GO was combined, the specific surface area and pore volume increased as compared with those of pristine GO and PTs, respectively. This increase in surface area may be attributed to the inhibition of reduced graphene oxide layer aggregation by the PTs sheet. BET analysis confirms that the augmented surface area in the nanocomposite is a result of the prevention of GO sheet folding in the layered structure. This result can be ascribed to the formation of 2D/2D heterostructure of rGO and PTs which leads to the volumetric expansion of pore. Therefore, it should be mentioned that the surface area, pore volume, and pore size characteristics of material structures are of great significance for the mass transfer process in pseudocapacitive processes.

The thermal stability of the samples was assessed using thermogravimetric analysis (TGA). TGA curves of PTs, rGO-PTs nanocomposite, and rGO-PTs nanocomposite after 4000 electrochemical cycles are shown in Fig. 5b. The pristine PTs exhibit thermal stability up to 144 °C, which is lower than that of the rGO-PTs nanocomposites, signifying a rapid degradation of PTs in the absence of rGO. Major degradation of PTs commences at 255 °C due to thermal decomposition. In contrast, the rGO-PTs nanocomposite, significant degradation initiates at a higher temperature range (148–260 °C). Moreover, the rGO-PTs nanocomposite shows increased weight retention of up to 19 % at 600 °C upon incorporating rGO, as opposed to the 4 % weight retention

observed for pristine PTs. The findings from the TGA curves clearly indicates both the decomposition temperature and residual weight are enhanced with the addition of rGO, demonstrating an improvement in the thermal stability of the rGO-PTs nanocomposite. This enhancement is attributed to rGO role in stabilizing the thermally degraded portions of PTs and acting as a barrier to the volatile components of PTs, thereby elevating the degradation temperature of the nanocomposite. After GCD testing (4000 cycles), the thermal response of the composite exhibited a higher rate of mass loss compared to both PTs and the as-prepared composite. This increased rate of mass loss is ascribed to the degradation of the rGO-PTs nanocomposite, due to the accumulation of sulphate ions during the charge–discharge process, a finding complemented by XPS data.

The electrochemical properties and charge storage mechanisms of redox pseudocapacitors are illustrated in Fig. 6 (b, c), focusing on as synthesized rGO-PTs nanocomposite. The pseudocapacitors store charge primarily through surface or bulk redox reaction occurring in the interfaces of reduced graphene oxide and polythiophene two-dimensional (2D/2D) sheets.

The observed similarities in their electrochemical profiles can be rationalized by the relationship between the electric potential and the quantity of charges generated either at the electrode/electrolyte interface or within the interface of rGO and PTs in rGO-PTs nanocomposite internal surface. This charge generation is follows adsorption and desorption processes.

It is important to note that materials cannot be categorized definitely as pseudocapacitive solely based on certain electrochemical

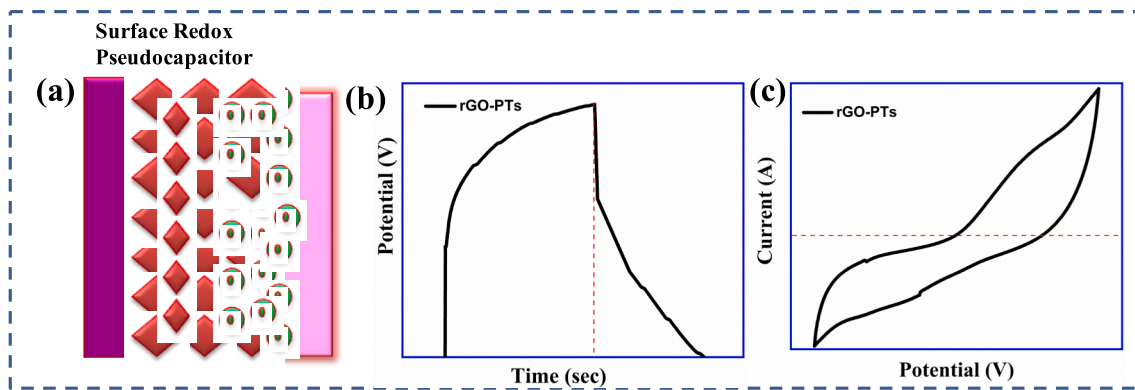


Fig. 6. Schematic illustration of the energy storage mechanisms of pseudocapacitors with their corresponding electrochemical signatures (a-c) shapes of CV and GCD curves.

characteristics. Consequently, it is not always appropriate to calculate capacitance values without clear pseudocapacitive signatures. Typically, the primary materials investigated for pseudocapacitive electrode applications are conducting polymers (CPs) and transition metal compounds (TMCs) [34–37]. These materials are known for their ability to undergo redox reactions that contribute to charge storage as pseudocapacitors.

4. Discussion

The electrochemical performance of the fabricated GO, PTs and rGO-PTs nanocomposite as supercapacitors was evaluated using electrochemical techniques *viz.* CV, GCD and EIS. The rGO-PTs/GCE electrode exhibit characteristic CV curves indicative of pseudocapacitor behaviour, which is attributed to the oxygen functional groups on the rGO surface.

For the pristine PTs/GCE, the electrochemical properties are predominantly associated with the intercalation of anions (Cl^-) from the electrolyte. However, in the reduced state of the nanocomposite, a negative charge accumulation occurs due to the presence of rGO, considering the PTs as neutral. The large, immobile rGO anions exert electrostatic repulsion on the electrons in the PTs, facilitating their removal and leading to a negative shift in the oxidation potential [38].

Fig. 7b displays CV curves obtained at various scan rates from 10 to 100 mV/s, where pair of distinct redox peaks is observed in the electrochemical window -0.2 to 1 V (Ag vs. Ag/AgCl). An increase in scan rate leads to enhanced intensity in the peak currents, suggesting the 2D/2D nanosheets promotes rapid redox reactions. Apparently, no redox peaks are observable in the pristine GO/GCE at a scan rate of 50 mV/s. The highest specific capacitance for the rGO-PTs/GCE is achieved at scan rate corresponding to 10 mV/s, and decreases with higher scan rates, possibly owing to diffusion limitations rGO-PTs/GCE pores, as shown in Fig. 7c. The CV curve of pristine GO and PTs at different scan rates is shown in Figure S6(a) and Figure S7 (a) of Supporting information.

Galvanostatic-charge–discharge (GCD) measurements were conducted on a three-electrode electrochemical cell in the electrochemical window -0.2 to 1 V, yielding capacitance measurements as depicted in Fig. 7d for GO/GCE, PTs/GCE, and rGO-PTs/GCE electrodes at a current density of 7.5 A/g. The specific capacitances are calculated and found to be 106.83 F/g, 64.98 F/g, and 131.13 F/g respectively. All three electrodes demonstrated capacitive behaviour with nearly symmetric charge–discharge curves. The addition of PTs altered the shape of the rGO-PTs/GCE curve from nearly symmetric to asymmetric, indicating a Faradic charge transfer processes in the capacitance behaviour of the rGO-PTs/GCE. The synergistic interaction between the rGO and PTs in rGO-PTs results in a specific capacitance of 1412 F/g even after 10000 cycles, calculated using Equation (1) at current density 7.5 A/g.

$$Cs = \frac{I\Delta t}{m\Delta V} \quad (1)$$

Cs is the specific capacitance (F/g) where I is the current density, Δt is the discharge time (s), ΔV is the potential change in the discharge process (V), and m is the mass of active material (g).

The GCD curves for rGO-PTs/GCE at various current densities are shown in Fig. 7(e, f), with specific capacitance values presented in Table 2. The observed decrease in capacitance with increasing current density is attributed to the slower progression of Faradic redox reactions compared to electric double-layer capacitance (EDLC), which suggests the rGO-PTs/GCE exhibits favourable power capability.

To investigate the factors contributing to the superior electrochemical performance of rGO-PTs/GCE, the electrode kinetics were analyzed. Supercapacitor electrodes typically operate through two distinct energy storage mechanisms: one involves the establishment of an electric double layer at the electrode/electrolyte interface (diffusion control process), while the other relies on the rapid redox reactions occurring at the electrode surface (capacitance control process). These modes can be differentiated using Equations (4) and Equations (5) [39].

$$i = av^b \quad (4)$$

$$\log(i) = \log(a) + b\log(v) \quad (5)$$

where i represents the current at the potentials represented in the inset of Fig. 8a, v represents the scan rate, a and b are constants. The value of b at different potentials can be obtained by plotting $\log(i)$ against $\log(v)$ as shown in Fig. 8a, value of $b = 0.5$ corresponds to the ideal diffusion-controlled Faradaic process. In contrast, $b = 1$ corresponds to the outer surface non-diffusion-controlled process (double layer phenomenon). The b values lie between 0.5 and 1 , meaning that the charge storage comes from both diffusion-controlled and capacitive (double layer) processes. From Fig. 8a, we have found the values of b neither exactly 0.5 nor 1 , thus, we conclude the charge storage to be of mixed type *i.e.*, capacitive and diffusion controlled which is in agreement with the Dunn's method [40]. The total current contribution at a potential is the sum of diffusive-controlled and capacitive currents which is defined by Equation (6), furthermore, the diffusion controlled process in the electrode reaction process at a certain scan rate is further quantified by the following equation:

$$i(V) = i_{\text{capacitive}} + i_{\text{diffusion}} = k_1v + k_2v^{1/2} \quad (6)$$

where $i(V)$ is the response current under potential, and $k_1v + k_2v^{1/2}$ correspond to the capacitance control process and the diffusion control process, respectively. k_1 and k_2 can be determined by the relationship between $i(v)/v^{1/2}$ and $v^{1/2}$, using Equation (7).

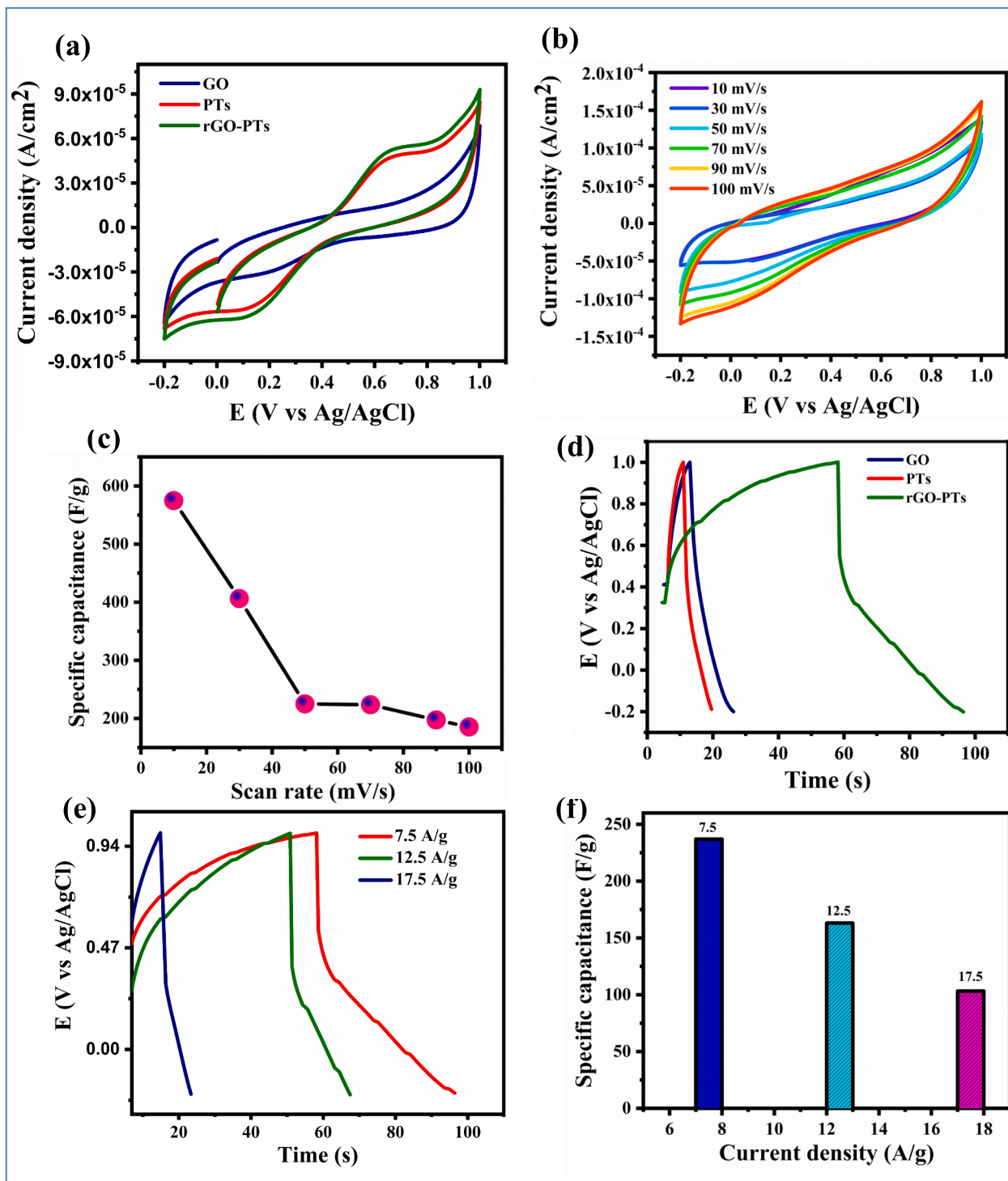


Fig. 7. (a) Comparative cyclic voltammograms (CV) for GO, PTs, rGO-PTs nanocomposite at 50 mV/s. (b) Scan rate studies for rGO-PTs in 2 M HCl at 10, 30, 50, 70, 90 and 100 mV/s and (c) The variation of specific capacitance with scan rate. (d) GCD curves of GO, PTs and rGO-PTs of modified electrodes. (e) CD curve of rGO-PTs at the different current density and (f) Specific capacitance as a function of current density in 2 M HCl.

Table 2

Specific capacitance of rGO-PTs at various current densities.

Current densities (A/g)	Specific capacitance (F/g)
7.5	317.61
12.5	234.15
17.5	146.37

$$\frac{i(\nu)}{\nu^{1/2}} = k_1 \nu^{\frac{1}{2}} + k_2 \quad (7)$$

Thus, the value of k_1 can be obtained by linear fitting of $i(V)/\nu^{1/2}$ vs $\nu^{1/2}$ at different voltages as shown in Fig. 8b. Further, calculations show the apparent diffusion coefficients of rGO-PTs/GCE are -3.910×10^{-4} and $6.110 \times 10^{-4} \text{ cm}^2/\text{s}$ for oxidative peaks and reductive peaks, (the data for the pristine sample GO/GCE and PTs/GCE are given in Figure S6 (b) and Figure S7 (b) respectively in the Supporting information).

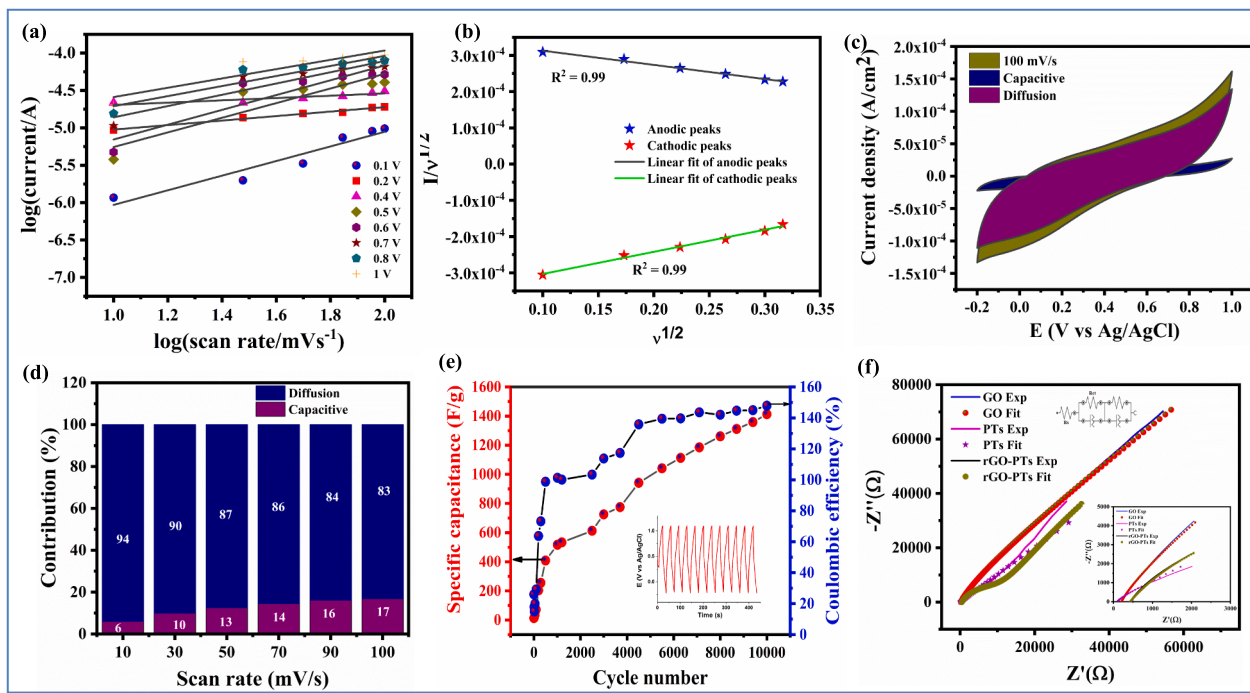


Fig. 8. (a) The determination of slope ("b") values at different potential regimes. (b) Linear relationship of anodic/cathodic peaks at different scan rates (10–100 mV/s). (c) Separation of the capacitive and diffusive currents at a scan rate of 100 mV/s (d) Bar diagram representing contribution ratios of capacitive and diffusive limited oxidation/reduction of rGO-PTs/GCE at various scan rates (10–100 mV/s). (e) Specific capacitance (left vs. bottom) and coulombic efficiency (right vs. bottom) at 7.5 A/g (insets show the charge/discharge cycles). (f) Nyquist plot for GO/GCE, PTs/GCE, and rGO-PTs/GCE electrodes.

Fig. 8c shows a graphical depiction of the current contributions attributed by the capacitive and diffusion-controlled processes at a sweep rate of 100 mV/s. The navy blue highlight signifies the diffusion contribution in the CV curve, while the purple colour represents the capacitive contribution. Detailed contributions for pristine graphene oxide (GO/GCE), polythiophene (PTs/GCE), and reduced graphene oxide-polythiophene nanocomposite (rGO-PTs/GCE) at various scan rates are depicted in Figure S8, S9, and S10, respectively in the Supporting information. The percentage of contributions from the capacitive and diffusive processes for different scan rates are for the rGO-PTs/GCE is illustrated in Fig. 8d. For the pristine GO/GCE and PTs/GCE are shown in Figure S6 (c) and Figure S7 (c) in the Supporting information. As can be seen from Fig. 8d, the increase in scan rate, decreases the diffusive contribution while the capacitive contribution increases. At the highest scan rate of 100 mV/s, the rGO-PTs/GCE electrode demonstrates a capacitive contribution of 83 % compared to a diffusive contribution of 17 %. The capacitive contribution is found increase in GO/GCE, PTs/GCE and rGO-PTs/GCE at the highest scan rate (100 mV/s) 2 times in case of GO/GCE and PTs/GCE and 3 times for rGO-PTs/GCE compared to the lowest scan rate (10 mV/s). This increasing capacitive contribution w.r.t increasing scan rate is attributed to the specific adsorption of charged species on the electrode surface. The specific adsorption of charged species starts contributing to the non faradic processes. Since in our CV study we found this adsorption fairly contributes as a barrier for the diffusion processes. These findings indicate a high diffusion-controlled ion intercalation process, resulting in a slow dynamic capacitance response in the capacitance control process. Lower scanning speeds allow sufficient time for the diffusion-controlled ion intercalation process, whereas higher scan rates lead to an expanded capacitive contribution. The diffusive-controlled process significantly influences the overall capacitance, especially at higher scan rates, highlighting the rapid transfer kinetics of rGO-PTs/GCE.

Stability tests for the rGO-PTs were conducted using GCD in a 2 M HCl solution, as depicted in Fig. 8e. A notable observation from these tests was the significant increase in specific capacitance with an

increasing number of cycles, as illustrated in Fig. 8e. The electrode underwent cycling for 10,000 cycles at a current density of 7.5 A/g. Initially, during the first 1000 cycles, the rGO-PTs/GCE performance improved, likely due to the electrochemical reduction of GO and the activation of the electrode material, resulting in a rapid capacitance increase. In the subsequent phase from 1000 to 10,000 cycles, a steady capacitance growth was observed. This trend could be attributed to the diminishing presence of oxygenated groups on the electrode surface as the reduction of GO continued. This hypothesis is supported by the XPS spectra as shown in Fig. 2. The core C 1 s spectra reveal a clear loss of oxygen functionality, and a dramatic decrease in the number of oxygenated groups is recorded in Table 1, possibly due to protonation processes associated with the electro reduction at lower pH values [41].

Electrochemical impedance spectroscopy (EIS) was employed to gain the insights into the internal resistance of the electrode material and the resistance within the electrolyte solution. Nyquist plots were generated over a frequency range of 100 mHz to 100 kHz, with the inset of Fig. 8f displaying the corresponding equivalent circuit. The rGO-PTs/GCE electrode demonstrates a vertical line in the low-frequency region, indicative of the capacitive behaviour. The electrode series resistance (R_s) at the high frequency end was comparable to that of GO/GCE, confirming the nature of GO as a high electronic conductivity and even retained after PTs loading. However, a small semi-circle, appears at low frequency region of PTs/GCE and rGO-PTs/GCE indicative of the charge transfer process of the pseudocapacitive electrode materials. The enlarge pattern of the high frequency region of pristine and nanocomposite is shown in Fig. 8f inset. GO acts as a new site for electrolyte interaction, shortens the ion diffusion pathway, and facilitates rapid conduction. The charge storage and transfer efficiency of GO is enhanced due to its low charge transfer resistance (R_{ct}) [42]. The GO electrode exhibited an R_{ct} of 734 Ω and R_s of 42 Ω , with no semicircle observed due to the materials high conductivity. The combination of these two materials in the nanocomposite led to a reduction in both the charge transfer resistance and the solution resistance, with values of 19 Ω and 223 Ω respectively, indicating lower resistance to ion movement

within the nanocomposites pores. The impedance data was evaluated by in-built electrochemical workstation (PGSTAT 302 N) software, where the equivalent circuit is shown in Fig. 8f inset. The equivalent circuit model fitting helped in determining the circuit component parameters comprising R_{ct} , solution resistance R_s , as summarized in Table S2 in the Supporting information. Additionally, Table 3 provides comparative data on the characteristics of various polymer-based carbonaceous composite materials used as supercapacitors.

To explore insights into the practical application of rGO-PTs electrodes, we fabricated an rGO-PTs//rGO-PTs symmetric supercapacitor (SSC) device and subjected it to electrochemical evaluation. The positive and negative electrodes were composed of rGO-PTs, while the gel electrolyte consisted of 2 M HCl with polyvinyl alcohol (PVA). This device, depicted in Fig. 9a, exhibited reasonable operating potential windows ranging from 1.0 to 0 V, respectively. Fig. 9b showcases the cyclic voltammetry (CV) curve of the rGO-PTs//rGO-PTs SSC at a working voltage of 1 V and various scan rates, maintaining a consistent and stable hybrid capacitor profile even at high scan rates, indicative of desirable electrochemical reversibility and rate characteristics. Additionally, Fig. 9c displays the galvanostatic charge–discharge (GCD) curve of the rGO-PTs//rGO-PTs SSC device within the range of 0–0.8 A/g, exhibiting high symmetry in charge and discharge, efficient reversibility, and rapid current–potential response. Upon increasing the voltage window beyond 0.8 V, the CV curve exhibited regular shape variations without polarization phenomena; however, for practical GCD testing, a voltage window of 0.8 V was chosen.

Notably, the GCD curve for rGO-PTs//rGO-PTs SSC at various current densities (0.2, 0.3, 0.4, 0.5, 0.6 A/g) yielded corresponding specific capacitances of 23, 166, 242, 293, and 167 F/g, respectively. Moreover, the device demonstrated commendable cycle stability at 0.3 A/g than other current densities because the charging time (T_C) is 10.62 s and discharge time (T_d) is 44.14 s (Fig. 9d), retaining an average capacitance of 99.4 % after 3000 charge–discharge cycles at a current density of 0.3 A/g. As shown in the inset of Fig. 9d, three rGO-PTs//rGO-PTs SSC devices in series can light up a red light-emitting diode for 4 s at a rated voltage of 2.5 V, demonstrating its competitive energy density. In summary, the rGO-PTs//rGO-PTs SSC electrode is a very promising supercapacitor for practical applications.

Fig. 9e shows the energy density vs power density plot (Ragone plot). The energy density (E; Wh/kg) is calculated using Equation (2) and the power density (P; W/kg) is derived from Equation (3),

$$E = \frac{1}{2} C (\Delta V)^2 \quad (2)$$

Where, C is the specific capacitance (F/g) and ΔV is the potential window.

$$P = \frac{3600E}{\Delta t} \quad (3)$$

Table 3

Comparison of electrolyte, cycle stability, and specific capacitance, of proposed supercapacitor with other reported supercapacitors.

Materials	Electrolyte	Cycle stability	Capacitance retention (%)	Specific capacitance (F/g)/(A/g)	Energy density (Wh/kg)	Power density (W/kg)	References
rGO/PTh/CB		1000	92.57	930.63	42.47	1532	[43]
PPy/GO-HT	1 M H ₂ SO ₄	3000	92	198	7.4	90	[44]
N-MWCNT/CMC	3 M KOH and PVA/H ₂ SO ₄	4000	96	274	18	—	[45]
P3HT/SWCNTs	0.1 M LiClO ₄	1000	805	245.8	50.8	308.7	[46]
PEDOT-MeOH /SWCNTs	1 M H ₂ SO ₄	5000	80	0.114	5.3	—	[47]
PD2ET/SWCNTs	1 M KCl	8000	91	399	22.5	—	[48]
S-Mxene/HG _{0.05}		10,000	96	446	14.84	250	[49]
rGO-PTs /GCE	2 M HCl	10,000	106	1412	8.94	4320	Present work

E is the energy density and Δt is the discharge time (s).

The Ragone plot (Fig. 9e) revealed a high energy density of 8.94 Wh/kg at a power density of 4320 W/kg, surpassing previously reported hybrid material systems, underscoring superior electrochemical performance. Furthermore, the Nyquist plot of the fabricated device (Fig. 9f) depicted a lower internal and diffusion resistances, indicating excellent conductivity of the device.

5. Conclusion

This study demonstrates that the swollen liquid crystalline lamellar mesophase (SLCLM) method is used effectively to synthesize 2D/2D rGO-PTs nanocomposites. The synthesized nanocomposite exhibits high electrochemical performance, especially after undergoing GCD cyclic stability for 10000 cycles, with enhanced specific capacitance. In terms of electrochemical properties, the rGO-PTs nanocomposite reached peak specific capacitance values of 1412 F/g at a current density of 7.5 A/g in a 2 M HCl electrolyte even after 10,000 cycles. The hybrid rGO-PTs nanocomposite manifests a pronounced synergistic effect, yielding higher capacitance compared to either graphene oxide (GO) or poly-thiophene (PTs) individually.

Moreover, the rGO-PTs display remarkable stability, retaining 106 % of the initial capacitance even after 10,000 charge/discharge cycles at room temperature. As the number of charge/discharge cycles increases, there is a corresponding increase in the number density of polarons within the composite, leading to an elevated negative charge density on the rGO-PTs/GCE surface. During charging, sulphur moieties in the polymer network become oxidized, with the rate of oxidation escalating as the number of cycles increases. The electrons generated in this process conducts through the π-bond network of the in-situ reduced sp² carbons of rGO and the PTs network. These electrons are then instrumental in reducing the oxygen within the composite, as evidenced by the XPS and Raman spectroscopy results. Finally, a symmetric supercapacitor (SSC) device of rGO-PTs//rGO-PTs is fabricated and electrochemically characterised which was able to light up a red LED for 4 s. which demonstrates the use of rGO-PTs//rGO-PTs SSC as a promising supercapacitor for practical applications.

Authors' contributions

KKS played a pivotal role in conceptualizing the synthesis method for the study. AKT was instrumental in optimizing and synthesizing the rGO-PTs and its pristine materials, working under the guidance of KKS and SNT. The electrochemical experiments were conducted by AKT and SNT, under the supervision of KKS. DPD contributed to the formal analysis of manuscript. SSM and CKH providing characterization. KKS provided overall supervision for the research project. All authors actively engaged in discussions throughout the research process and collectively wrote the manuscript for final communication.

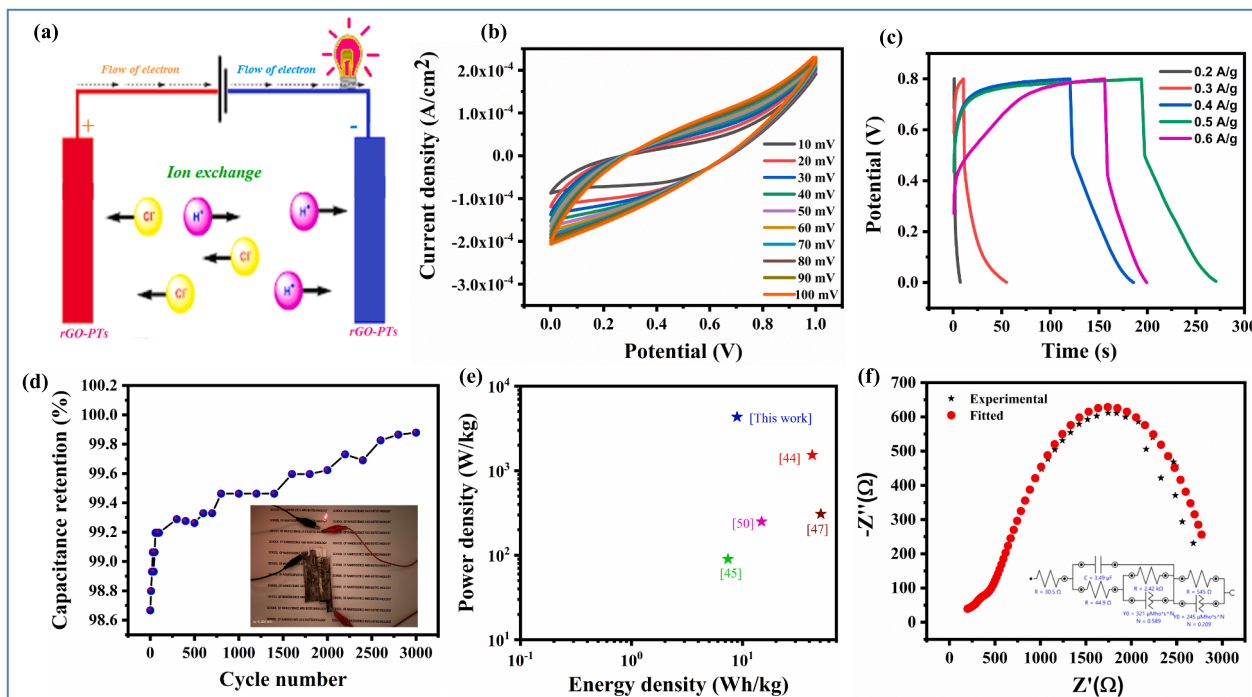


Fig. 9. (a) Schematics of symmetric supercapacitor (SSC) designed by rGO-PTs. (b) CV curves of rGO-PTs // rGO-PTs SSC at different scan rate (10–100 mV/s). (c) GCD curves of rGO-PTs // rGO-PTs SSC at different current densities. (d) Cycling test of rGO-PTs // rGO-PTs SSC at 0.3 A/g. (e) Ragone plot of rGO-PTs and (f) rGO-PTs // rGO-PTs SSC fitting equivalent Circuit.

CRediT authorship contribution statement

Anita K. Tawade: Writing – original draft, Visualization, Methodology, Formal analysis, Data curation. **Shivaji N. Tayade:** Writing – review & editing, Supervision, Methodology, Formal analysis. **Deepak P. Dubal:** Formal analysis. **Sawanta S. Mali:** Resources. **Chang Kook Hong:** Resources. **Kiran Kumar K. Sharma:** Writing – review & editing, Supervision, Project administration, Methodology, Investigation, Conceptualization.

Declaration of competing interest

The authors declare that they have no known competing financial interests or personal relationships that could have appeared to influence the work reported in this paper.

Data availability

Data will be made available on request.

Acknowledgments

Anita Tawade is thankful to Chhatrapati Shahu Maharaj Research, Training and Human Development Institute (SARTHI), Pune for providing CSMNRF-SRF-2019. Prof. Dr. Kiran Kumar Sharma is thankful to State Project Directorate -RUSA Centre for Nanofabrics (D.3.P.43.12) for financial support.

Appendix A. Supplementary data

Supplementary data to this article can be found online at <https://doi.org/10.1016/j.cej.2024.151843>.

References

- [1] Q. Wang, J.Y. Yan, G. Wang, Z. Fan, T. Wei, J. Cheng, M. Zhang, X. Jing, Template synthesis of hollow carbon spheres anchored on carbon nanotubes for high rate performance supercapacitors, Carbon 52 (2013) 209–218, <https://doi.org/10.1016/j.carbon.2012.09.022>.
- [2] Q. Cheng, J. Tang, J. Ma, H. Zhang, N. Shinya, L.C. Qin, Graphene and nanostructured MnO₂ composite electrodes for supercapacitors, Carbon 49 (2011) 2917–2925, <https://doi.org/10.1016/j.carbon.2011.02.068>.
- [3] A.K.C. Gallegos, M.E. Rincón, Carbon nanofiber and PEDOT-PSS bilayer systems as electrodes for symmetric and asymmetric electrochemical capacitor cells, J. Power Sources 162 (2006) 743–747, <https://doi.org/10.1016/j.jpowsour.2006.06.085>.
- [4] W. Li, J. Chen, J. Zhao, J. Zhang, J. Zhu, Application of ultrasonic irradiation in preparing conducting polymer as active materials for supercapacitor, Mater. Lett. 59 (2005) 800–803, <https://doi.org/10.1016/j.matlet.2004.11.024>.
- [5] Z. Huang, H. Zhou, C. Li, F. Zeng, C. Fu, Y. Kuang, Preparation of well-dispersed PdAu bimetallic nanoparticles on reduced graphene oxide sheets with excellent electrochemical activity for ethanol oxidation in alkaline media, J. Mater. Chem. 22 (2012) 1781–1785, <https://doi.org/10.1039/C1JM13024B>.
- [6] K. Tadyszak, J.K. Wychowaniec, J. Litowczenco, Biomedical applications of graphene-based structures, Nanomaterials 8 (2018) 944, <https://doi.org/10.3390/nano8110944>.
- [7] S.C. Han, J.L. Quan, F.G. Zhou, Y.H. Xue, N. Li, F.Y. Li, D. Wang, 3D printing of architected graphene-based aerogels by cross-linking GO inks with adjustable viscoelasticity for energy storage devices, Rare Met. 42 (2023) 971–981, <https://doi.org/10.1007/s12598-022-02202-y>.
- [8] M. Lee, T.W. Kim, C.Y. Park, K. Lee, T. Taniguchi, K. Watanabe, M.G. Kim, D. K. Hwang, Y.T. Lee, Graphene bridge heterostructure devices for negative differential transconductance circuit applications, Nano-Micro Letters 15 (2023) 22, <https://doi.org/10.1007/s40820-022-01001-5>.
- [9] A. Zarepour, S. Ahmadi, N. Rabiee, A. Zarrabi, S. Iravani, Self-healing MXene-and graphene-based composites: properties and applications, Nano-Micro Letters 15 (2023) 100, <https://doi.org/10.1007/s40820-023-01074-w>.
- [10] S. Stankovich, R.D. Pineri, S.T. Nguyen, R.S. Ruoff, Synthesis and exfoliation of octanate-treated graphene oxide nanoplatelets, Carbon 44 (2006) 3342–3347, <https://doi.org/10.1016/j.carbon.2006.06.004>.
- [11] H. Wang, L. Ma, M. Gan, T. Zhou, X. Sun, W. Dai, H. Wang, S. Wang, Design and assembly of reduced graphene oxide/polyaniline/urchin-like mesoporous TiO₂ spheres ternary composite and its application in supercapacitors, Compos. B Eng 92 (2016) 405–412, <https://doi.org/10.1016/j.compositesb.2016.02.047>.
- [12] S.U. Rahman, P. Röse, M. Surati, A.U.H.A. Shah, U. Kreuer, S. Bilal, 3D polyaniline nanofibers anchored on carbon paper for high-performance and light-weight supercapacitors, Polymers 12 (2020) 2705, <https://doi.org/10.3390/polym12112705>.
- [13] I. Benchikh, A.O. Ezzat, L. Sabantina, Y. Benmimoun, A. Benyoucef, Investigation of hybrid electrodes of polyaniline and reduced graphene oxide with bio-waste-

- derived activated carbon for supercapacitor applications, *Polymers* 16 (2024) 421, <https://doi.org/10.3390/polym16030421>.
- [14] A.U.H.A. Shah, S. Ullah, S. Bilal, G. Rahman, H. Seema, Reduced graphene oxide/poly (pyrrole-co-thiophene) hybrid composite materials: Synthesis, characterization, and supercapacitive properties, *Polymers* 12 (2020) 1110, <https://doi.org/10.3390/polym12051110>.
- [15] W. Wang, W. Lei, T. Yao, X. Xia, W. Huang, Q. Hao, X. Wang, One-pot synthesis of graphene/SnO₂/PEDOT ternary electrode material for supercapacitors, *Electrochim. Acta* 108 (2013) 118–126, <https://doi.org/10.1016/j.electacta.2013.07.012>.
- [16] A.B. Rohom, P.U. Londhe, J.I. Han, N.B. Chaire, Conducting polymer wrapped SnO₂/RGO nanocomposite: An efficient high-performance supercapacitor material, *Surf. Interfaces* 44 (2024) 103605, <https://doi.org/10.1016/j.surfin.2023.103605>.
- [17] Q. Li, B. Guo, J. Yu, J. Ran, B. Zhang, H. Yan, J.R. Gong, Highly efficient visible-light-driven photocatalytic hydrogen production of CdS-cluster-decorated graphene nanosheets, *J. Am. Chem. Soc.* 133 (2012) 10878–10884, <https://doi.org/10.1021/ja2025454>.
- [18] D.C. Marcano, D.V. Kosynkin, J.M. Berlin, A. Sinitskii, Z. Sun, A. Slesarev, L. B. Alemany, W. Lu, J.M. Tour, Improved synthesis of graphene oxide, *ACS Nano* 4 (2010) 4806–4814, <https://doi.org/10.1021/mn1006368>.
- [19] B. Gillet, D.J. Nicole, J.J. Delpuech, The hydroxyl group protonation rates of α , β and γ -cyclodextrins in dimethyl sulphoxide, *Tetrahedron Lett.* 23 (1982) 65–68, [https://doi.org/10.1016/S0040-4039\(00\)97533-6](https://doi.org/10.1016/S0040-4039(00)97533-6).
- [20] H. Bao, L. Wang, C. Li, J. Luo, Structural characterization and identification of graphdiyne and graphdiyne-based materials, *ACS Appl. Mater. Interfaces* 11 (2018) 2717–2729, <https://doi.org/10.1021/acsami.8b05051>.
- [21] X. Gao, H. Liu, D. Wang, J. Zhang, Graphdiyne: synthesis, properties, and applications, *Chem. Soc. Rev.* 48 (2019) 908–936, <https://doi.org/10.1039/C8CS00773J>.
- [22] M.P. Down, S.J. Rowley-Neale, G.C. Smith, C.E. Banks, Fabrication of graphene oxide supercapacitor devices, *ACS Applied Energy Materials* 1 (2018) 707–714, <https://doi.org/10.1021/acsam.7b00164>.
- [23] S.H. Aboutalebi, A.T. Chidembo, M. Salari, K. Konstantinov, D. Wexler, H.K. Liu, S. X. Dou, Comparison of GO, GO/MWCNTs composite and MWCNTs as potential electrode materials for supercapacitors, *Energ. Environ. Sci.* 4 (2011) 1855–1865, <https://doi.org/10.1039/C1EE01039E>.
- [24] W. Chu, Y. He, Y.S. Chu, L. Meng, J. Liu, H. Qin, S. Tao, A highly stable Cu (OH)₂ poly (vinyl alcohol) nanocomposite membrane for dramatically enhanced direct borohydride fuel cell performance, *J. Power Sources* 467 (2020) 228312, <https://doi.org/10.1016/j.jpowsour.2020.228312>.
- [25] R. Singh, A.K. Bajpai, A.K. Shrivastava, CdSe nanorod-reinforced poly (thiophene) composites in designing energy storage devices: study of morphology and dielectric behavior, *Polym. Bull.* 78 (2021) 115–131, <https://doi.org/10.1007/s00289-020-03104-8>.
- [26] G.S. Gund, D.P. Dubal, S.B. Jambure, S.S. Shinde, C.D. Lokhande, Temperature influence on morphological progress of Ni (OH)₂ thin films and its subsequent effect on electrochemical supercapacitive properties, *J. Mater. Chem. A* 1 (2013) 4793–4803, <https://doi.org/10.1039/C3TA00024A>.
- [27] N.M.S. Hidayah, W.W. Liu, C.W. Lai, N.Z. Noriman, C.S. Khe, U. Hashim, and H.C. Lee, Comparison on graphite, graphene oxide and reduced graphene oxide: Synthesis and characterization, In AIP conference proceedings 1892 (2017), AIP Publishing. <https://doi.org/10.1063/1.5005764>.
- [28] A.C. Ferrari, D.M. Basko, Raman spectroscopy as a versatile tool for studying the properties of graphene, *Nat. Nanotechnol.* 8 (2013) 235–246, <https://doi.org/10.1038/nano.2013.46>.
- [29] Q.T. Vu, M. Pavlik, N. Hebestreit, U. Rammelt, W. Plieth, J. Pfleger, Nanocomposites based on titanium dioxide and polythiophene: structure and properties, *React. Funct. Polym.* 65 (2005) 69–77, <https://doi.org/10.1016/j.reactfunctpolym.2004.11.011>.
- [30] Y. Shen, F.E. Chen, P. Wu, G. Shi, A two-dimensional Raman spectroscopic study on the structural changes of a polythiophene film during the cooling process, *J. Chem. Phys.* 119 (2003) 11415–11419, <https://doi.org/10.1063/1.1622661>.
- [31] Z. Niu, Y. Zhang, Y. Zhang, X. Lu, J. Liu, Enhanced electrochemical performance of three-dimensional graphene/carbon nanotube composite for supercapacitor application, *J. Alloy. Compd.* 820 (2020) 153114, <https://doi.org/10.1016/j.jallcom.2019.153114>.
- [32] C. Li, X. Chen, L. Shen, N. Bao, Revisiting the oxidation of graphite: Reaction mechanism, chemical stability, and structure self-regulation, *ACS Omega* 5 (2020) 3397–3404, <https://doi.org/10.1021/acsomega.9b03633>.
- [33] K.K. Jhankal, M.S. Khan, D. Jhankal, K. Sachdev, Electrochemical evaluations of reduced graphene oxide for efficient counter electrode in dye-sensitized solar cell, *Journal of Electrochemical Science and Engineering* 13 (2023) 1051–1061, <https://doi.org/10.5599/jese.1977>.
- [34] C. Choi, J.H. Kim, H.J. Sim, J. Di, R.H. Baughman, S.J. Kim, Microscopically buckled and macroscopically coiled fibers for ultra stretchable supercapacitors, *Adv. Energy Mater.* 7 (2017) 1602021, <https://doi.org/10.1002/aenm.201602021>.
- [35] L. Cao, J. Zhu, Y. Li, P. Xiao, Y. Zhang, S. Zhang, S. Yang, Ultrathin single-crystalline vanadium pentoxide nanoribbon constructed 3D networks for superior energy storage, *J. Mater. Chem. A* 2 (2014) 13136–13142, <https://doi.org/10.1039/C4TA02229G>.
- [36] Q. Ke, C. Guan, X. Zhang, M. Zheng, Y.W. Zhang, Y. Cai, H. Zhang, J. Wang, Surface charge mediated formation of HTiO₂@ Ni (OH)₂ heterostructures for high performance supercapacitors, *Adv. Mater.* 29 (2017) 1604164, <https://doi.org/10.1002/adma.201604164>.
- [37] P. Yu, Z. Zhang, L. Zheng, F. Teng, L. Hu, X. Fang, A novel sustainable flour derived hierarchical nitrogen doped porous carbon/polyaniline electrode for advanced asymmetric supercapacitors, *Adv. Energy Mater.* 6 (2016) 1601111, <https://doi.org/10.1002/aenm.201601111>.
- [38] C. Zhu, J. Zhai, D. Wen, S. Dong, Graphene oxide/polypyrrole nanocomposites: one-step electrochemical doping, coating and synergistic effect for energy storage, *J. Mater. Chem.* 22 (2012) 6300–6306, <https://doi.org/10.1039/C2JM16699B>.
- [39] S. Song, X. Ma, W. Li, B. Zhang, B. Shao, X. Chang, X. Liu, Novel stylophora coral-like furan-based Ni/Co bimetallic metal organic framework for high-performance capacitive storage and non-enzymatic glucose electrochemical sensing, *J. Alloy. Compd.* 931 (2023) 167413, <https://doi.org/10.1016/j.jallcom.2022.167413>.
- [40] M.Z. Iqbal, M.M. Faisal, M. Sulman, S.R. Ali, A.M. Afzal, M.A. Kamran, T. Alharbi, Capacitive and diffusive contribution in strontium phosphide-polyaniline based supercapacitry, *J. Storage Mater.* 29 (2020) 101324, <https://doi.org/10.1016/j.est.2020.101324>.
- [41] M. Zhou, Y. Wang, Y. Zhai, J. Zhai, W. Ren, F. Wang, S. Dong, Controlled synthesis of large area and patterned electrochemically reduced graphene oxide films, *Chemistry—A European Journal* 15 (2009) 6116–6120, <https://doi.org/10.1002/chem.200900596>.
- [42] G. Lian, S. Dong, Electrochemical behaviour of Fe (CN) 63–/4– redox ions in a polypyrrole film, *J. Electroanal. Chem. Interfacial Electrochem.* 260 (1989) 127–136, [https://doi.org/10.1016/0022-0728\(89\)87104-9](https://doi.org/10.1016/0022-0728(89)87104-9).
- [43] M. Ates, C. Alperen, Polythiophene-based reduced graphene oxide and carbon black nanocomposites for supercapacitors, *Iran. Polym. J.* 32 (2023) 1241–1255, <https://doi.org/10.1007/s13726-023-01201-9>.
- [44] A. Moyssewicz, K. Pajak, K. Gajewska, G. Gryglewicz, Synthesis of polypyrrole/reduced graphene oxide hybrids via hydrothermal treatment for energy storage applications, *Materials* 13 (2020) 2273, <https://doi.org/10.3390/ma13102273>.
- [45] P.K. Basivi, S. Ramesh, V. Kakani, H.M. Yadav, C. Bathula, N. Afsar, A. Sivasamy, H.S. Kim, V.R. Pasupuleti, H. Lee, Ultrasound-mediated nitrogen-doped multivalved carbon nanotubes involving carboxy methylcellulose composite for solid-state supercapacitor applications, *Sci. Rep.* 11 (2021) 9918, <https://doi.org/10.1038/s41598-021-89430-x>.
- [46] A. Shokry, M. Karim, M. Khalil, S. Ebrahim, J. El Nady, Supercapacitor based on polymeric binary composite of polythiophene and single-walled carbon nanotubes, *Scientific Reports* 12 (2022) 11278, <https://doi.org/10.1038/s41598-022-15477-z>.
- [47] Y. Zhang, H. Zhang, F. Jiang, W. Zhou, R. Wang, J. Xu, X. Duan, Y. Wu, Y. Ding, Electrochemical assembly of homogenized poly (3, 4-ethylenedioxythiophene methanol)/SWCNT nano-networks and their high performances for supercapacitor electrodes, *Ionics* 26 (2020) 3631–3642, <https://doi.org/10.1007/s11581-020-03475-y>.
- [48] M. Zhou, Y. Li, Q. Gong, Z. Xia, Y. Yang, X. Liu, J. Wang, Q. Gao, Polythiophene grafted onto single wall carbon nanotubes through oligo (ethylene oxide) linkages for supercapacitor devices with enhanced electrochemical performance, *ChemElectroChem* 6 (2019) 4595–4607, <https://doi.org/10.1002/celec.201901074>.
- [49] Z. Cai, Y.F. Ma, M. Wang, A.N. Qian, Z.M. Tong, L.T. Xiao, S.T. Jia, X.Y. Chen, Engineering of electrolyte ion channels in MXene/holey graphene electrodes for superior supercapacitive performances, *Rare Met.* 41 (2022) 2084–2093, <https://doi.org/10.1007/s12598-021-01935-6>.